

This is a repository copy of *In situ X-ray diffraction measurement of shock-wave-driven twinning and lattice dynamics*.

White Rose Research Online URL for this paper:

<https://eprints.whiterose.ac.uk/123828/>

Version: Accepted Version

---

**Article:**

Wehrenberg, C. E., McGonegle, David, Bolme, C. et al. (13 more authors) (2017) In situ X-ray diffraction measurement of shock-wave-driven twinning and lattice dynamics. *Nature*. pp. 496-499. ISSN 0028-0836

<https://doi.org/10.1038/nature24061>

---

**Reuse**

Items deposited in White Rose Research Online are protected by copyright, with all rights reserved unless indicated otherwise. They may be downloaded and/or printed for private study, or other acts as permitted by national copyright laws. The publisher or other rights holders may allow further reproduction and re-use of the full text version. This is indicated by the licence information on the White Rose Research Online record for the item.

**Takedown**

If you consider content in White Rose Research Online to be in breach of UK law, please notify us by emailing [eprints@whiterose.ac.uk](mailto:eprints@whiterose.ac.uk) including the URL of the record and the reason for the withdrawal request.

# Femtosecond measurement of shock wave driven twinning and lattice dynamics

**Authors:** C. E. Wehrenberg,<sup>1\*</sup> D. McGonegle,<sup>2</sup> C. Bolme,<sup>3</sup> A. Higginbotham,<sup>4</sup> A. Lazicki,<sup>1</sup> H.J. Lee,<sup>5</sup> B. Nagler,<sup>5</sup> H.-S. Park,<sup>1</sup> B. A. Remington,<sup>1</sup> R. E. Rudd,<sup>1</sup> M. Sliwa,<sup>2</sup> M. Suggit,<sup>2</sup> D. Swift,<sup>1</sup> F. Tavella,<sup>5</sup> L. Zepeda-Ruiz,<sup>1</sup> and J.S. Wark<sup>2</sup>

## Affiliations:

<sup>1</sup>*Lawrence Livermore National Laboratory, 7000 East Ave., Livermore CA 94550 USA.*

<sup>2</sup>*Department of Physics, Clarendon Laboratory, University of Oxford, Parks Road, Oxford, OX1 3PU, United Kingdom.*

<sup>3</sup>*Los Alamos National Laboratory, Bikini Atoll Road, SM-30, Los Alamos, NM 87545, USA*

<sup>4</sup>*University of York, Department of Physics, Heslington, York YO10 5DD, United Kingdom*

<sup>5</sup>*SLAC National Accelerator Laboratory, 2575 Sand Hill Rd, Menlo Park, CA 94025, USA*

\*Correspondence to: [wehrenberg1@llnl.gov](mailto:wehrenberg1@llnl.gov)

Understanding the deformation and associated defects created by shock waves is crucial in a wide range of fields, such as planetary formation and asteroid impact sites<sup>1-3</sup>, formation of interstellar dust clouds<sup>4</sup>, ballistic penetrators<sup>5</sup>, spacecraft shielding<sup>6</sup>, and ductility in high-performance ceramics<sup>7</sup>. Shock waves in solid materials can cause extreme damage and deformation. Twinning and dislocation-slip are the basic mechanisms of plastic deformation at the lattice level, yet diagnosing the active mechanism *in-situ* has been elusive. Methods for characterizing lattice defects have typically been limited to ex-post-facto experiments<sup>8-11</sup>, which examine the microstructures of samples and are complicated by post-shock annealing<sup>12</sup> and reverberations. In addition measurements have been limited to relatively modest pressures. *In-situ* X-ray diffraction (XRD) experiments have provided new insights into dynamic material behavior<sup>13</sup> but are only starting to be applied to plasticity during shock compression<sup>14-17</sup>, and have yet to provide detailed insight into competing deformation mechanisms. Here we present XRD experiments with femtosecond resolution that apply crystallographic techniques to capture *in-situ*, lattice-level pictures of the microstructural processes driving shock deformation. Tantalum, an important material for high-energy density physics applications, serves as a model body-centered cubic (BCC) material. For shock-compressed Ta, where simulations<sup>18-20</sup> and previous experiments<sup>8-12</sup> provide conflicting information on the dominant mechanism, we report twinning and related lattice rotation occurring on the time scale of tens of picoseconds. Despite a common association between twinning and strong shocks<sup>21</sup>, we also find a transition from twinning to slip-dominated plasticity at high pressure (<150 GPa), a regime recovery experiments cannot accurately access. As the role of *in-situ* diffraction for studying shock waves and other high-rate phenomena continues to grow, the texture analysis techniques demonstrated here will be useful in studying a broad range of processes induced by plasticity.

Prior *in-situ* experimental measurements of lattice evolution during shock measurements have not had sufficient time or spatial resolution to make critical direct comparisons to theory. The need for a more direct comparison to theory is evident since, even for a well-studied BCC metal such as Ta, existing experiments can disagree on the operative deformation mechanism, twinning versus dislocation generation and transport (slip). Ta samples show significant twinning at shock pressures above  $\sim 50$  GPa<sup>8-11</sup>, whereas previous *in-situ* diffraction experiments have not registered a signal indicative of twinning at these pressures<sup>16,17</sup>. While the wide difference in timescales makes comparing between experiments difficult, large-scale molecular dynamics (MD) simulations in strongly shocked Ta also disagree. The deformation mechanism varies from slip<sup>18</sup> to twinning<sup>19</sup> to a combination of the two mechanisms<sup>20</sup>, depending on which interatomic potential is used in the simulation. In this study the new capabilities offered by x-ray free-electron laser sources are used to make direct comparisons to molecular dynamics simulations.

Here we use temporally resolved, *in-situ* x-ray diffraction to probe shocked polycrystalline Ta, providing direct characterization of the mechanism and time scale of the ultrafast deformation for shock pressures from 10 GPa to shock melt ( $\sim 300$  GPa). The experiments were performed at the Matter in Extreme Conditions end station of the Linac Coherent Light Source, and a sketch of the setup is shown in Figure 1. Probed during the initial shock transit through the Ta, the diffraction patterns have signal from both driven and undriven material. The material transitions rapidly to the shocked state. The low signal level between driven and undriven lines implies a fast transition, occurring on timescales of  $<100$  ps for the highest pressures ( $>10^9$  s<sup>-1</sup> strain rate).

The Ta foil was fabricated by vapor deposition, which creates a fiber-like texture where the grains share a common crystallographic direction along the sample normal ([110] in this case) but are oriented randomly in the transverse direction. Having a known, highly-textured starting material means new orientations created by deformation can be readily observed in the diffraction data<sup>22</sup>. Twinning and slip produce distinct changes to the texture of the Ta sample that can be used to determine the active mechanism for deformation during shock compression. Both twinning and slip can cause a rotation of the lattice when the sample is laterally confined during shock compression, since a lattice rotation is needed to maintain the geometry of uniaxial compression<sup>23</sup>. However, twinning also produces an additional mirror rotation in the twin grain.

Due to the highly-textured structure of the Ta foil, only certain spots are visible on the powder Debye diffraction ring. The azimuthal positions of the spots correspond to the angles of the respective diffraction planes. Figure 2 shows an example diffraction pattern taken prior to shock loading. Contours of constant  $\chi$ -angle, the angle between the sample surface and the diffraction plane, are overlaid on the figure (constant  $2\theta$  is shown with dashed lines). Two sketches of a Ta unit cell demonstrate that the  $\{110\}$  planes will occupy angles of  $60^\circ$  or  $90^\circ$  relative to the sample plane. The  $\{110\}$  diffraction ring has texture spots at corresponding  $\chi$  of  $60^\circ$  and  $90^\circ$  (marked with green arrows). Similar reasoning accounts for the azimuthal positions of texture spots for the other diffraction rings.

Texture changes are evident in the driven data for a wide range of shock pressures, as shown in the example diffraction patterns in Figure 3. Comparing  $\chi$  for the compressed and uncompressed spots reveals the texture change during shock compression. In Fig. 3a (23 GPa), the d-spacing, the distance between lattice planes, decreases in the driven

portion of the sample and the diffraction lines move to higher  $2\theta$  angles, but no change in  $\chi$  is observed. At 46 GPa (Fig. 3b), a new set of spots forms on the compressed Debye ring, marked with red arrows, that correspond to an orientation for twinning across a  $\{112\}$  mirror plane (the dominant twin plane in BCC Ta). In the higher-pressure data (Fig 3c and d), the  $\chi = 60^\circ$  spot is elongated azimuthally; the texture spot spans the detector gap in Fig. 3c and even splits into two spots (Fig. 3d). These changes in  $\chi$  correspond to lattice rotation, where the rotation moves some planes to higher  $\chi$  and other planes to lower  $\chi$ . In contrast, no shift in  $\chi$  is expected for the  $\chi = 90^\circ$  spot since the rotation occurs in this plane.

The amount of texture change is plotted in Fig. 4a (twinning) and 4b (lattice rotation). The twin fraction is minimal (consistent with zero) below 25 GPa, and increases with shock pressure in the 25-75 GPa regime, reaching a twin fraction of  $\sim 30\text{-}40\%$  at 75 GPa. Surprisingly, even though twinning is often associated with strongly driven metals, at higher shock pressures ( $>150\text{-}175$  GPa), the twin fraction falls to low levels ( $< 10\%$ ). The lattice rotation in Fig. 4b can be due to either slip or twinning and is found to increase monotonically. Thus the decrease in twin fraction observed above  $\sim 150$  GPa indicates a transition to slip-dominated plasticity.

Figure 4c plots the equivalent plastic strain associated with twinning,  $\gamma_{Tw}^P$  (orange triangles) and lattice rotation,  $\gamma_{Ro}^P$  (purple diamonds), while the plastic strain from slip can be determined from the difference between  $\gamma_{Ro}^P$  and  $\gamma_{Tw}^P$ . The total strain for a given shock is shown by  $\gamma_{Hu}^P$  (black line), the equivalent plastic strain on the Hugoniot. If either mechanism dominates the response, the plastic strain from that mechanism will be a large fraction of  $\gamma_{Hu}^P$ . While the onset of twinning occurs at 25 GPa, the plastic response is twin-dominated in the 40-80 GPa range. Above 150 GPa, the plastic strain from twinning falls well below the Hugoniot, indicating the plastic response becomes slip-dominated.

The trend for the lattice rotation follows the Hugoniot with a small offset. There is a difference of 4% strain between the two curves,  $\gamma_{Hu}^P - \gamma_{Ro}^P \sim 0.04$ , indicated by the dashed line in Fig 4c. In Fig. 4 b-d, the  $\chi = 90^\circ$  spots of the driven (110) Debye rings show some azimuthal broadening. Since, as noted above, slip along  $\{112\}$  planes does not affect the (110)  $\chi = 90^\circ$  planes, this broadening is an indication of a small amount of slip along other planes and likely accounts for the 4% difference.

Phase transformations can also create texture changes and should be considered as a possible response to shear strain<sup>22</sup>. While density functional theory indicates the BCC phase is the stable phase for pressures up to 700 GPa and temperatures up to the melt line<sup>24</sup>, the plastic deformation of shock compression may drive a transition to the omega phase, as indicated by recovery and MD simulations<sup>2,25</sup>. Our data does not show significant amounts ( $>0.1\%$ ) of omega phase (see ED Fig. 1 & ED Fig. 2) or any other solid phase apart from BCC for all pressures, from ambient up to melt at  $\sim 300$  GPa.

We performed MD simulations using the Ravelo potential<sup>26</sup>, simulating a Ta single crystal at 300 K shocked along the [110] direction. Figure 4a shows the simulated twin fraction and Fig. 4b shows the simulated lattice rotation as a function of pressure (black circles). The MD simulations show the onset of twinning occurring at similar pressures as the data, although the decrease in twin fraction occurs at much lower pressure in the simulations. The simulated lattice rotation is in good agreement with the data in the 75-200 GPa

pressure range.

The quantitative measurements provided by XRD allow direct comparison to simulations and modeling. Complex constitutive models like the Livermore Multiscale Model<sup>27</sup> begin with the assumption that plasticity is dislocation based. Even in the simplified case studied here, where no phase transformations occur and loading is restricted to a single crystal axis, the dominant deformation mechanism transitions multiple times, from minimal twinning to twinning-dominated to slip-dominated, as the shock pressure is increased. Approaching similar timescales to simulations and exploring high pressure regimes that are difficult to observe and interpret in *ex-post-facto* experiments, these results highlight the importance and growing role of *in-situ* experiments in studying materials in extreme conditions.

**Fig. 1. Experimental configuration used at the MEC end station at LCLS for shock compression and *in-situ* x-ray diffraction.** A shock wave is driven by laser ablation into a plastic ablator and Ta foil with a (110) fiber texture. The shock compressed Ta is probed by the LCLS beam and the resulting diffraction patterns are collected on an array of CSPADs.

**Fig. 2. Example x-ray diffraction data from (110) fiber textured Ta prior to shock loading.** A sketch of the diffraction geometry describes  $2\theta$ , the Bragg angle, and  $\chi$ , the angle between the sample normal and diffraction plane normal. For a sample with (110) texture, {110} planes have  $\chi=60^\circ, 90^\circ$ . The diffraction data have corresponding {110} texture spots at those  $\chi$  angles, marked with green arrows. Solid curves indicate constant  $\chi$  corresponding to specific lattice planes [for {110}:  $\chi=60^\circ, 90^\circ$ ; for {200}:  $\chi=90^\circ, 45^\circ$ ; for {211}:  $\chi=73^\circ, 54.7^\circ$ ]. The dashed curves indicate constant  $2\theta$ .

**Fig. 3. Diffraction patterns from Ta shock compressed at (a) 19, (b) 44, (c) 108, and (d) 169 GPa.** The driven spots appear at higher diffraction angle, which appears as a shift upwards in this view. Lines of constant  $\chi$  -angle are shown at  $60^\circ$  and  $90^\circ$  to illustrate the reorientation of the texture spots in the driven Ta. At 23 GPa (a) no reorientation is observed, since the driven and undriven diffraction spots have the same azimuthal location. At 46 GPa, new texture spots arise corresponding to twinning across a {112} mirror plane plus an additional  $2.5^\circ$  rotation. At higher pressures, (c) and (d), large lattice rotations are observed, causing the  $\chi=60^\circ$  (110) spot (marked with red arrows) to elongate and then split.

**Fig. 4. Twin fraction, rotation and plastic strain computed from the diffraction data.** (a) Twin fraction as a function of shock pressure measured by the ratio of texture spots (orange triangles) and from MD simulations (black circles). (b) Lattice rotation angle from XRD (purple diamonds) and from MD simulations (black circles). (c) Equivalent plastic strain inferred from lattice rotation (purple diamonds) and twin fraction (orange triangles). The equivalent plastic strain on the Hugoniot is plotted (black line). The rotation data follows the Hugoniot line minus 4% strain (dotted line). Twinning accounts for the majority of the Hugoniot plastic strain in the 40-80 GPa range (pink shaded region is a guide to the eye), but falls well below the Hugoniot above 150 GPa (blue shaded region), indicating the response is slip dominated.

## References:

1. Ashworth, J. R. & Schneider, H. Deformation and Transformation in Experimentally Shock-Loaded Quartz. *Phys. Chem. Minerals*. **11**, 241 (1985).

- 181  
182 2. French, B. & Koeberl, C. The convincing identification of terrestrial meteorite impact  
183 structures: What works, what doesn't, and why. *Earth Sci. Rev.* **98**, 123-170 (2010).  
184  
185 3. Gattacceca, J., Lamali, A., Rochette, P., Boustie, M. & Berthe, L. The effects of explosive-  
186 driven shocks on the natural remanent magnetization and the magnetic properties of rocks. *Phys.*  
187 *Earth and Planet. Inter.* **162**, 85-98 (2007).  
188  
189 4. Draine, B. T. & Salpeter, E. E. Destruction mechanisms for interstellar dust. *Astrophys. J.* **231**,  
190 438-455 (1979).  
191  
192 5. Pappu, S., Kennedy, C., Murr, L. E., Magness, L. S. & Kapoor, D. Microstructure analysis and  
193 comparison of tungsten alloy rod and [001] oriented columnar-grained tungsten rod ballistic  
194 penetrators. *Mat. Sci. & Eng. A.* **262**, 115-128 (1999).  
195  
196 6. Thoma, K., Schafer, F., Hiermaier, S. & Schneider, E. An approach to achieve progress in  
197 spacecraft shielding. *Adv. Space Res.* **34**, 1063-1075 (2004).  
198  
199 7. Chen, M. W., McCauley, J. W., Dandekar, D. P. & Bourne, N. K. Dynamic plasticity and  
200 failure of high-purity alumina under shock compression. *Nature Mater.* **5**, 614-618 (2006).  
201  
202 8. Murr, L.E. *et al.* Shock-induced deformation twinning in tantalum. *Acta Mat.* **45**, 157-175  
203 (1996).  
204  
205 9. Hsiung, L. L. & Lassila, D. H. Shock-induced deformation twinning and omega  
206 transformation in tantalum and tantalum-tungsten alloys. *Act. Mat.* **48**, 4851-4865 (2000).  
207  
208 10. Lu, C. H. *et al.* Laser compression of monocrystalline tantalum. *Acta Mat.* **60**, 6601-  
209 6620 (2012).  
210  
211 11. Florando, J. N., Barton, N. R., El-Dasher, B. S., McNaney, J. M. & Kumar, M. Analysis  
212 of deformation twinning in tantalum single crystals under shock loading conditions. *J. Appl.*  
213 *Phys.* **113**, 083522 (2013).  
214  
215 12. Lu, C. H. *et al.* Laser compression of nanocrystalline tantalum. *Acta Mat.* **61**, 7767-7780  
216 (2013).  
217  
218 13. Loveridge-Smith, A. *et al.* Anomalous elastic response of silicon to uniaxial shock  
219 compression on nanosecond time scales. *Phys. Rev. Lett.* **86**, 2349-2352 (2001).  
220  
221 14. Suggit, M. J. *et al.* Nanosecond white-light Laue diffraction measurements of dislocation  
222 microstructure in shock-compressed single-crystal copper. *Nature Comm.* **3**, 1224 (2012).  
223  
224 15. Milathianaki, D. *et al.* Femtosecond visualization of lattice dynamics in shock-  
225 compressed matter. *Science* **342**, 220-223 (2013).  
226

16. Comley, A. J. *et al.* Strength of shock-loaded single-crystal tantalum [100] determined using *in-situ* broadband *Phys. Rev. Lett.* **110**, 115501 (2013).
17. Wehrenberg, C. E. *et al.* Lattice-level observation of the elastic-to-plastic relaxation process with subnanosecond resolution in shock-compressed Ta using time-resolved in situ Laue diffraction. *Phys. Rev. B* **92**, 104305 (2015).
18. Rudd, R. E. *et al.* Theory and simulation of 1D to 3D plastic relaxation in tantalum. *AIP Conf. Proc.* **1426**, 1379 (2012).
19. Higginbotham, A. *et al.* Molecular dynamics simulations of shock-induced deformation twinning of a body-centered-cubic metal. *Phys. Rev. B* **88**, 104105 (2013).
20. Tramontina, D. *et al.* Molecular dynamics simulations of shock-induced plasticity in tantalum. *High Energy Den. Phys.* **10**, 9 (2014).
21. Meyers, M. "Plastic deformation in shock waves" in *Dynamic Behavior of Materials* (John Wiley and Sons, Inc., New York, 1994).
22. McGonegle, D., Milathianaki, D., Remington, B. A., Wark, J. S. & Higginbotham, A., Simulations of in situ X-ray diffraction from uniaxially compressed highly textured polycrystalline targets. *J. Appl. Phys.* **118**, 065902 (2015).
23. Fleischer, R. L. Single crystal lattice rotation during compression. *J. Mech. Phys. Solids* **6**, 301-306 (1958).
24. Miljacic, L., Demers, S., Hong, Q.-J. & van de Walle, A. Equation of state of solid, liquid and gaseous tantalum from first principles. *CALPHAD* **51**, 133-143 (2015).
25. Lu, C. H., Hahn, E. N., Remington, B. A., Maddox, B. R. & Meyers, M. A. Phase transformation in tantalum under extreme laser deformation. *Sci. Rep.* **5**, 15064 (2015).
26. Ravelo, R., Germann, T. C., Guerrero, O., An, Q. & Holian, B. L. Shock-induced plasticity in tantalum single-crystal: Interatomic potentials and large-scale molecular-dynamics simulations. *Phys. Rev. B* **88**, 134101 (2013).
27. Barton, N. R. *et al.* A multiscale strength model for extreme loading conditions. *J. Appl. Phys.* **109**, 073501 (2011).

**Acknowledgments:** We thank P. Mirkarimi and C. Davis for their work in preparing the targets. This work was performed under the auspices of the U.S. Department of Energy by Lawrence Livermore National Laboratory under Contract No. DE-AC52-07NA27344, and Los Alamos National Laboratory under Contract No. DE-AC52-06NA25396. Use of the Linac Coherent Light Source (LCLS), SLAC National Accelerator Laboratory, is supported by the U.S. Department of Energy, Office of Science, Office of Basic Energy Sciences under Contract No.



DE-AC02-76SF00515. The MEC instrument is supported by the U.S. Department of Energy, Office of Science, Office of Fusion Energy Sciences under contract No. SF00515. This material is based upon work supported by the U.S. Department of Energy, Office of Science, Office of Fusion Energy Sciences, under Award Number DE-SCW-1507. JSW is grateful to the UK EPSRC for support under grant EP/J017256/1. D.M. was supported by LLNS under contract number B595954.

**Author contributions:** The experiments were conceived by C.E.W., D. M., B.A.R., A. H., M.J.S., R.E.R. and J.S.W., and were performed by C.E.W., D. M., B.A.R., A. H., J.S.W., H.-S.P, D.S., A.L., C. B., H.J.L., B. N., and F. T. The data were analyzed by C.E.W., D. M., A.L. and M.S. and the results were interpreted by C.E.W., D.M., M.J.S., A. H., B.A.R., J.S.W., and R.E.R. Molecular dynamics simulations were performed by D.M., A.H., L.Z.-R., and R.E.R. The manuscript was written by C.W., B.A.R, R.E.R, J.S.W., and D.M.

**Author Information:** Reprint and permission information is available at [www.nature.com/reprints](http://www.nature.com/reprints). The authors declare no competing financial interests. Readers are welcome to comment on the online version of the paper. Correspondence and requests for materials should be addressed to C.E.W ([wehrenberg1@llnl.gov](mailto:wehrenberg1@llnl.gov)).

## 290 Methods

291 The experiments were performed at the Matter in Extreme Conditions (MEC) end station of  
 292 the Linac Coherent Light Source (LCLS). The Ta structure was probed while under shock  
 293 compression and the resulting diffraction patterns were recorded on several Cornell-SLAC  
 294 hybrid Pixel Array Detectors (CSPADs)<sup>27</sup>, as shown in Fig. 1. A planar shock was driven by  
 295 direct laser ablation from frequency doubled (527 nm) laser beams, using a 5-10 ns square pulse.  
 296 Hybrid phase plates were used to modify the focal spot. These plates use surface features to shift  
 297 the phase of the light, creating focal spots of 100 μm, 150 μm or 250 μm diameter with “top-hat”  
 298 intensity profiles. Each target consisted of a 50 μm thick kapton ablator glued to a 6 μm thick  
 299 foil of Ta. The ablator thickness (several times larger than the sample) prevents reverberations  
 300 from entering the Ta before the initial shock has passed through the sample. The thickness of the  
 301 ablator also helps to smooth out spatial variations in drive created by speckle pattern of the laser  
 302 spot. The Ta foil was fabricated by vapor deposition onto a SiO<sub>2</sub> substrate at a temperature  
 303 (~450°C) sufficient both to create the body-centered cubic (BCC) α-Ta phase and to delaminate  
 304 the Ta from the substrate upon cooling. Small amounts (<0.5%) of β phase are also present in  
 305 some of the Ta samples.

306 A Velocity Interferometer System for Any Reflector (VISAR) diagnostic was used to  
 307 monitor the free surface velocity of the Ta during the shock compression and release and  
 308 help set the diffraction timing. The optical streak camera system (line VISAR) was used to  
 309 confirm the planarity of the drive. The VISAR images show the planar driven region  
 310 approximately corresponds to the size of the phase plates, and this planar region larger than the  
 311 20-μm x-ray beam. An example of the VISAR data for a 130 GPa shock is shown in ED Fig 3.

312 The LCLS x-ray beam was tuned for 9.6 keV photons in a 50 fs pulse. The diffraction angles  
 313 were calibrated using a powder sample of LaB<sub>6</sub> and CeO<sub>2</sub> standards. The calibrated detector  
 314 positions were then used to measure the diffraction angles from the Ta samples. The sample  
 315 orientation is determined by fitting the  $\chi$  of the spots of the ambient diffraction pattern. The  
 316 amount of lattice rotation can then be determined from the  $\chi$  of the driven spots. A single  
 317 rotation from the original [110] orientation is determined that best fits the measured  $\chi$  of the  
 318 driven spots. The diffracted intensity was adjusted to account for polarization of the x-ray beam  
 319 using the following factor:

$$320 \quad P = (\cos^2 \phi * \cos 2\theta)^2 + \sin^2 \phi \quad P = [\cos^2 \phi * \cos(2\theta)]^2 + \sin^2 \phi$$

321 where  $\phi$  is the azimuthal angle for diffracted x-rays. The pressure produced by the shock loading  
 322 was calculated from the d-spacing measured by diffraction assuming BCC structure.  
 323 Specifically, the shock pressure was found using the shock speed data from Mitchell and  
 324 Nellis<sup>28</sup>,  $U_s = C_0 + S * U_p$  where  $C_0 = 3293$  m/s and  $S=1.307$ , which together with the Rankine-  
 325 Hugoniot equations, give the following expression for the shock pressure<sup>29</sup>:

$$326 \quad P_x = \rho_0 C_0^2 \frac{1 - (d/d_0)^3}{1 - S[1 - (d/d_0)^3]} \quad P_x = \rho_0 C_0^2 (1 - [d/d_0]^3) / (1 - S[1 - (d/d_0)^3])$$

327 where  $\rho_0$  is the initial density and  $d_0$  and  $d$  are the initial and compressed lattice spacings. Since  
 328 the error in determining the peak positions in the diffraction data is small, the main sources of  
 329 uncertainty in determining the pressure are the spatial and temporal non-uniformity in the drive.  
 330 These non-uniformities will not significantly change the average pressure, but may affect the  
 331 range of pressures present in the sample. The VISAR records show that the drive is steady prior

to the first reverberation. Some spatial non-uniformity is present but is small over the 20  $\mu\text{m}$  region probed by the x-ray beam. Based on uncertainty in fitting the peak positions, the pressure uncertainty is +/- 3 GPa.

For high pressure shots, where the driven diffraction pattern had the diffuse signal indicative of a liquid sample, the pressure could not be reliably measured from the diffraction data. The pressure estimate from the laser ablation intensity is consistent with previous measurements of the shock melting pressure, ~300 GPa<sup>30</sup>.

### Expected signal if omega phase ( $\omega$ ) were present

We have analyzed the diffraction data for the presence of omega ( $\omega$ ) phase. This phase has been observed in shock-recovered Ta samples by Hsiung and Lassila<sup>2</sup> and Lu et al.<sup>25</sup>. Hsiung provides the following relationship between the BCC and hexagonal lattice parameters:

$$a_{\omega} = \sqrt{2}a_{\alpha}, c_{\omega} = \frac{\sqrt{3}}{2}a_{\alpha} \quad a_{\omega} = \sqrt{2}a_{\alpha}, c_{\omega} = \sqrt{3}/2a_{\alpha}$$

where  $a_{\alpha}$  is the lattice parameter of the BCC phase, and  $c_{\omega}$  and  $a_{\omega}$  correspond to the omega phase. Lu et al. were able to match their TEM diffraction pattern using these lattice parameters. Lu et al. reported observing  $\omega$  phase in samples that are recovered following shock loading to ~70 GPa. In ED Fig 1. we show our driven data for a 73 GPa shock and indicate the expected peak positions for the hexagonal structure as well as the “rumpled” hexagonal structure reported by Hsiung and Lassila.

Since the initial ta structure is highly textured, the transformed omega phase may also be highly textured. Lu et al. state that they observed the same orientation relationship between the matrix and omega phase as Hsiung and Lassila, namely that the  $(111)_{\text{m}} // (0001)_{\omega}$  and  $[110]_{\text{m}} // [1000]_{\omega}$  where m refers to the matrix BCC phase and  $\omega$  is the transformed omega phase.

Using this relationship, we show in ED Fig. 2. the azimuthal positions of the texture spots for the omega phase (white lines). For simplicity, the rumpled structure is not shown. The detectors cover multiple spots where the omega peaks would be expected given the previously reported orientation relationships yet no signal was observed.

### Twin fraction calculation

We have measured the twin fraction by comparing the intensity of texture spots corresponding to the twin orientation with the intensity of other driven and undriven texture spots. In addition, the differing multiplicities of various planes associated with specific  $\chi$  must be considered. For example, a unit cell in the twin orientation will have twice as many planes for  $\chi = 90^\circ$  than  $\chi = 70.5^\circ$ , so that the twin fraction is given by,

$$f_{\text{TW}} = \frac{2 * I_{\text{Drvn}(110)\chi=70.5}}{I_{\text{Drvn}(110)\chi=90}} \quad f_{\text{TW}} = (2 * I_{\text{Drvn}(110)\chi=70.5}) / (I_{\text{Drvn}(110)\chi=90})$$

where  $I$  refers to the integrated intensity of the specified diffraction spot. This equation assumes azimuthal symmetry, since the two spots being compared have different azimuthal positions. The azimuthal variation of the (110) fiber texture was not known prior to the experiments, so the variation is a source of uncertainty in our measurements. Pole figure measurements were performed on remaining samples, and azimuthal lineouts, normalized relative to the azimuthal average, follow a roughly sinusoidal pattern with 180° rotational symmetry and variation in intensity of +/- 30%.

Similar calculations were performed for the (200)  $\chi=76.3^\circ$  and (211)  $\chi=61.3^\circ$  twin spots, and the results were averaged to arrive at the final twin fraction values. The error bars were set to the standard deviation of the measurements using the three lines. For shock pressures in the 50-150 GPa range, some of the driven twin spots fall into gaps between the detectors, limiting measurements in this pressure regime. The error was assumed to be 50% when twin spots were measured on only one diffraction line, which reflects the uncertainty in the azimuthal texture in both the twin spot and the reference spot.

We can quantitatively determine the role of twinning in the overall plastic response by comparing the plastic strain from twinning,  $\gamma_{Tw}^P$ , to the total plastic strain imparted by the shock,  $\gamma_{Hu}^P$ . Eqs. (1) and (2) give the two plastic strain quantities:

$$\gamma_{Tw}^P = f_{Tw} * \epsilon_0 * M \quad \gamma_{Tw}^P = f_{Tw} * \epsilon_0 * M \quad (1)$$

$$\gamma_{Hu}^P = 2/3 \ln\left(\frac{V_0}{V}\right) \quad \gamma_{Hu}^P = 2/3 \ln(V_0/V) \quad (2)$$

where  $f_{Tw}$  is the twin fraction,  $\epsilon_0$  is the eigenstrain, and  $M$  is the Schmid factor (for [110] loading,  $\epsilon_0 = 0.707$  and  $M = 0.471$ ), and  $V_0$  and  $V$  are the specific volumes in the ambient and shocked conditions respectively<sup>31,21</sup>. We have taken the residual elastic shear strain to be negligible due to the absence of diffraction ring distortion (discussed below), implying full plastic relaxation of the shear stress on the ultrashort time scale of the experiment.

The {112} planes serves as the dominant plane for both slip and twinning, meaning both mechanisms will produce similar lattice rotations. The observed rotation, found by fitting the azimuthal position of the diffraction spots, provides a measurement of the plastic strain caused by both mechanisms,  $\gamma_{Ro}^P$ , as shown by Eq (3),

$$\gamma_{Ro}^P = \ln\left(\frac{\cos \chi}{\cos \chi_0}\right) \quad \gamma_{Ro}^P = \ln(\cos \chi / \cos \chi_0) \quad (3)$$

where  $\chi_0$  and  $\chi$  correspond to the initial and final angles between the slip plane normal and the compression direction.

## How the plastic strain is calculated as a function of rotation

Here we discuss the relation between the plastic strain and the rotation that is measured. Throughout this analysis we assume that the residual shear stress in the shocked Ta is zero or so small that it can be neglected. This assumption, justified by the ring distortion analysis in the next section, allows us to impose that the elastic strain in the shocked state is strictly hydrostatic.

$$\epsilon_x^e + \epsilon_y^e + \epsilon_z^e = \ln\left(\frac{V}{V_0}\right) \quad \epsilon_x^e + \epsilon_y^e + \epsilon_z^e = \ln(V/V_0)$$

$$\epsilon_x^e = \epsilon_y^e = \epsilon_z^e = 1/3 \ln\left(\frac{V}{V_0}\right) \quad \epsilon_x^e = \epsilon_y^e = \epsilon_z^e = 1/3 \ln(V/V_0)$$

where  $\epsilon_x^e$  is the elastic strain in the shock direction and  $\epsilon_y^e$  and  $\epsilon_z^e$  are the transverse elastic strains. Similarly, we assume the plastic strains do not change the volume

$$\epsilon_x^p + \epsilon_y^p + \epsilon_z^p = 0 \quad \epsilon_x^p + \epsilon_y^p + \epsilon_z^p = 0$$

That uniaxial compression of crystals produces a rotation of the lattice is well known, and the rotation as function of compression is<sup>23</sup>

$$\epsilon_x^p = \ln \left( \frac{\cos \chi_0}{\cos \chi} \right) \quad \epsilon_x^p = \ln(\cos \chi / \cos \chi_0)$$

where  $\chi$  and  $\chi_0$  give the angle between the slip plane normal and the compression direction and  $\epsilon_x^p$  is the plastic strain along the compression direction.

Since the material is laterally constrained and compressed along the high symmetry [110] direction, we assume that, while individual grains may expand or contract in different transverse directions, the area of each grain transverse to the sample normal will remain the same. Thus we find that the total strain in the two transverse directions remains the same:

$$\epsilon_y^e + \epsilon_y^p + \epsilon_z^e + \epsilon_z^p = 0 \quad \epsilon_y^e + \epsilon_y^p + \epsilon_z^e + \epsilon_z^p = 0$$

$$\epsilon_x^p = \epsilon_y^e + \epsilon_y^p = \frac{2}{3} \ln \left( \frac{V}{V_0} \right) \quad \epsilon_x^p = \epsilon_y^e + \epsilon_y^p = 2/3 \ln(V/V_0)$$

therefore

$$\frac{\cos \chi_0}{\cos \chi} = \left( \frac{V}{V_0} \right)^{2/3} \quad \cos \chi_0 / \cos \chi = (V/V_0)^{2/3}$$

$$\gamma_p = -\frac{2}{3} \ln \left( \frac{V}{V_0} \right) = \ln \frac{\cos \chi}{\cos \chi_0} \quad \gamma_p = -2/3 \ln(V/V_0) = \ln(\cos \chi / \cos \chi_0)$$

For the (211) slip plane,  $\chi_0 = 54.7$

### Residual Elastic Shear Stress

We have analyzed the Debye rings for deviations from circularity that would indicate shear stress in the shocked state. When using the Hugoniot jump conditions to calculate the pressure from the measured d-spacing, or when calculating the equivalent plastic strain, we have assumed that the residual elastic shear stress is near zero. Residual elastic shear strain would mean that the strain is anisotropic, with higher elastic strain in the compression direction (shock propagation direction) and less in the transverse direction. This anisotropic elastic strain would manifest as a Debye-ring distorted by varying d-spacing, making it appear elliptical<sup>32</sup>. With no shear strain, the Debye-ring has constant  $2\theta$ . As shear strain increases, the driven rings move to higher  $2\theta$  for low  $\chi$  (right side of the diffraction pattern) and to lower  $2\theta$  for high  $\chi$  (left side of the diffraction pattern). While 0% strain produces a good fit to the data, small shear strains may also match.

We find at 2-3% shear strain, the data no longer provides a good match. Thus the assumption that the elastic shear strain is negligible is likely valid.

### **Molecular Dynamics Simulations**

Molecular dynamics simulations were performed using the LAMMPS code<sup>33</sup> and the Ravelo potential<sup>26</sup> for 100x100x800 unit cells (330x330x2644 Å). A portion of the end of sample is used as a piston. That section is “frozen” so that it won't respond to external forces and then ramped up to a set velocity to drive the shock. By performing a 3D Fourier Transform<sup>34</sup> of the plastically deformed region behind the shock front, we can find the average rotation of the crystal lattice about the [1-10] axis. The Per Atom Structure Factor (PASf) code<sup>12</sup> was used to determine the twin fraction in the same region.

**Data Availability.** The datasets generated and analyzed during the current study are available from the authors on reasonable request.

27. Philipp, H. T., Hromalik, M., Tate, M., Koemer, L. & Gruner, S. M. Pixel array detector for X-ray free electron laser experiments. *Nucl. Instrum. Methods Phys. Res. A* **649**, 67 (2011).

28. Mitchell, A. C. & Nellis, W. J. Shock compression of aluminum, copper and tantalum. *J. Appl. Phys.* **52**, 3363 (1981).

29. Meyers, M. “Shock Waves: Equations of State” in *Dynamic Behavior of Materials* (John Wiley and Sons, Inc., New York, 1994).

30. Brown, J. M. & Shaner J. W. in *Shock Waves in Condensed Matter*—1983, ed. J. R. Asay et al. (Elsevier, New York, 1984), p. 91.

31. Kalidindi, S. R. Incorporation of deformation twinning in crystal plasticity models. *J. Mech. Phys. Solids.* **46**, 267-290 (1998).

32. Higginbotham, A. & McGonegle, D. Prediction of Debye-Scherrer diffraction patterns in arbitrarily strained samples. *J Appl Phys.* **115**, 174906 (2014).

33. Plimpton, S. Fast parallel algorithms for short-range molecular dynamics. *J. Comput. Phys.* **117**, 1-19 (1995).

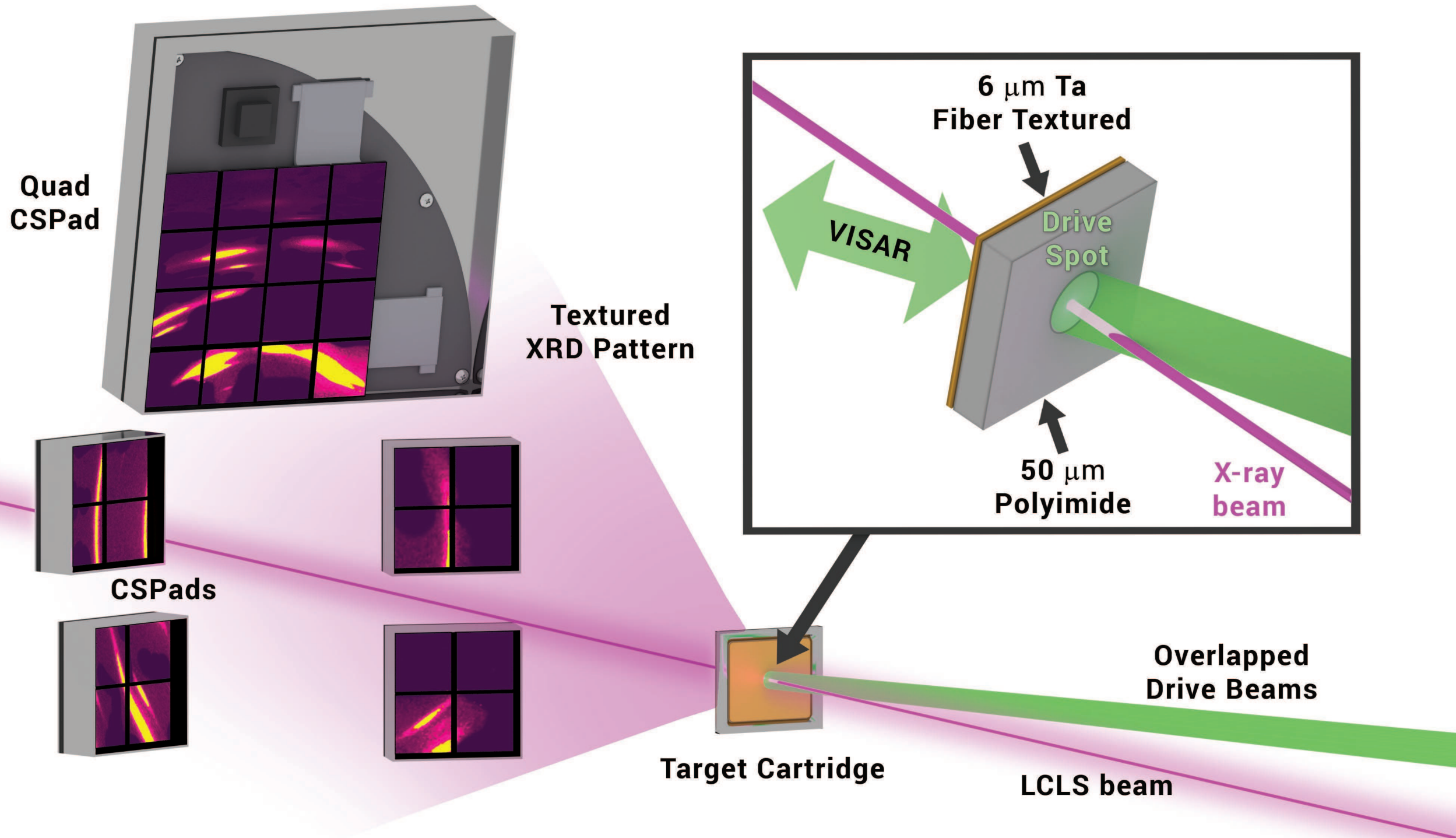
34. Kimminau, G. *et al.* Simulating picosecond x-ray diffraction from shocked crystals using post-processing molecular dynamics calculations. *J. Phys.: Condens. Matter* **20**, 505203 (2008).

482  
483  
484  
485  
486  
487  
488  
489  
490  
491  
492  
493  
494  
495  
496  
497  
498  
499  
500  
501  
502  
503

ED Fig. 1. Diffraction angle ( $2\theta$ ) plotted vs. x-ray counts averaged over  $2\pi$  in azimuthal angle for a shock pressure of 73 GPa. The indices of the ambient pattern, matching BCC with lattice parameter of  $a=3.308 \text{ \AA}$ , are marked in green. The driven pattern (black dots) match BCC with  $a=3.051 \text{ \AA}$ . Indexed peak positions for the hexagonal phase are marked with red lines, and peaks corresponding to the “rumples” structure observed by Hsiung & Lasilla<sup>2</sup> are marked with an asterisk. Both BCC and omega phase overlap the observed peaks, but additional peaks are expected for the omega phase that are not observed.

ED Fig. 2. Diffraction pattern for 73 GPa shock showing raw data (left) and overplotted with BCC and omega phase (right). The ambient BCC phase is marked with blue. Compressed and rotated BCC phase is marked in black, and the expected positions of the omega phase are marked in white.

ED Fig. 3. Example VISAR streak image for a 130 GPa shot using a  $250 \text{ }\mu\text{m}$  phase plate. The planar region of the shock, roughly similar in dimensions to the phase plate size, breaks out of the Ta free surface at 7.4 ns. The x-ray beam probes a  $20 \text{ }\mu\text{m}$  region in the center of the planar shock.





Sample  
Normal

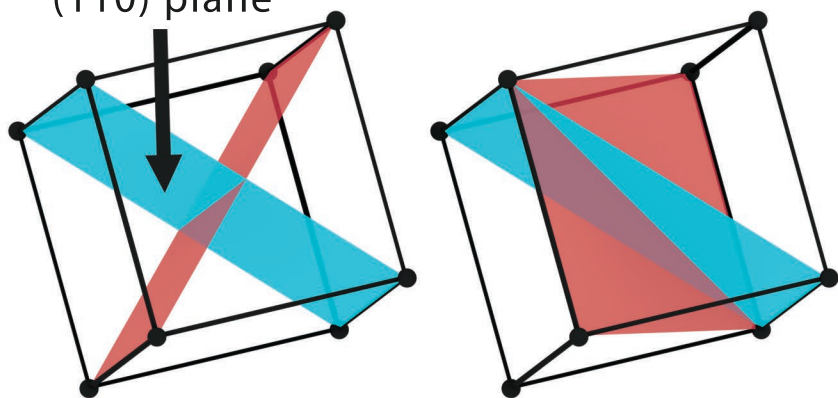
Plane  
Normal

$C$

$2q$

(110) Texture

Sample || to  
(110) plane



$C=90^\circ$   $C=60^\circ$

